AGU PUBLICATIONS

JGR

Journal of Geophysical Research: Atmospheres

RESEARCH ARTICLE
10.1002/2013JD020582

Key Points:
- Estimating Change in climate feedback by composition of cloud
- Separating climate feedback into several component using climate kernels
- Computing climate feedback using global climate model

Correspondence to:
Y.-S. Choi,
ysc@ewha.ac.kr

Citation:
Choi, Y.-S., C.-H. Ho, C.-E. Park, T. Storelvmo, and I. Tan (2014), Influence of cloud phase composition on climate feedbacks, *J. Geophys. Res. Atmos.*, *119*, 3687–3700, doi:10.1002/2013JD020582.

Received 19 JUL 2013
Accepted 10 MAR 2014
Accepted article online 13 MAR 2014
Published online 4 APR 2014

Influence of cloud phase composition on climate feedbacks

Yong-Sang Choi[1], Chang-Hoi Ho[2], Chang-Eui Park[2], Trude Storelvmo[3], and Ivy Tan[3]

[1]Department of Environmental Science and Engineering, Ewha Womans University, Seoul, Korea, [2]School of Earth and Environmental Sciences, Seoul National University, Seoul, Korea, [3]Department of Geology and Geophysics, Yale University, New Haven, Connecticut, USA

Abstract The ratio of liquid water to ice in a cloud, largely controlled by the presence of ice nuclei and cloud temperature, alters cloud radiative effects. This study quantitatively examines how the liquid fraction of clouds influences various climate feedbacks using the NCAR Community Atmosphere Model (CAM). Climate feedback parameters were calculated using equilibrated temperature changes in response to increases in the atmospheric concentration of carbon dioxide in CAM Version 3.0 with a slab ocean model. Two sets of model experiments are designed such that cloud liquid fraction linearly decreases with a decrease in temperature down to −20°C (Experiment "C20") and −40°C (Experiment "C40"). Thus, at the same subzero temperature, C20 yields fewer liquid droplets (and more ice crystals) than C40. Comparison of the results of experiments C20 and C40 reveals that experiment C20 is characterized by stronger cloud and temperature feedbacks in the tropics (30°N–30°S) (by 0.25 and −0.28 W m^{-2} K^{-1}, respectively) but weaker cloud, temperature, and albedo feedbacks (by −0.20, 0.11, and −0.07 W m^{-2} K^{-1}) in the extratropics. Compensation of these climate feedback changes leads to a net climate feedback change of ~7.28% of that of C40 in the model. These results suggest that adjustment of the cloud phase function affects all types of feedbacks (with the smallest effect on water vapor feedback). Although the net change in total climate feedback is small due to the cancellation of positive and negative individual feedback changes, some of the individual changes are relatively large. This illustrates the importance of the influence of cloud phase partitioning for all major climate feedbacks, and by extension, for future climate change predictions.

1. Introduction

The role of clouds in climate forcings and feedbacks remains one of the greatest uncertainties in climate prediction. In order to improve the representation of clouds in current climate models, various aspects of aerosol-cloud-precipitation interactions and cloud dynamics were recently incorporated [*Storelvmo et al.,* 2008; *Bretherton and Park,* 2009; *Lohmann and Hoose,* 2009; *Gettelman et al.,* 2012]. The inclusion of such improved cloud parameterizations may affect the major climate feedbacks of global climate models through changes in cloud, water vapor, lapse rate, and surface albedo in response to surface temperature changes [*Intergovernmental Panel on Climate Change*, 2007], which in turn affects the climate sensitivity of these models [*Li and Le Treut,* 1992; *Senior and Mitchell,* 1993; *Ho et al.,* 1998]. This is because cloud processes can influence all sources of feedback, not just the cloud-climate feedback. Here, we address the question of how the relative roles of the major climate feedbacks can be altered by cloud parameterizations. In particular, we focus on the treatment of cloud phase partitioning.

Knowledge of the relative proportion of liquid and ice within mixed-phase cloud layers is critical for the calculation of cloud radiative properties [*Choi et al.,* 2010a]. The importance of cloud phase arises because the characteristics of scattering and absorption of liquid particles are completely different from those of ice particles [*Liou,* 2002]. Moreover, mixed-phase clouds are ubiquitous in the Earth's middle and high troposphere, and their phase composition may change in the presence of ice-nucleating aerosols such as mineral dust [*Choi et al.,* 2010a, 2010b]. The resulting changes in cloud optical properties are known to have a potentially large impact on radiative transfer in the atmosphere [*Tsushima et al.,* 2006; *Gettelman et al.,* 2012].

Recently, the treatment of the partitioning of liquid and ice in clouds has become more sophisticated in many models. Some models attempt to explicitly represent ice nucleation processes; however, others still do not take ice nucleation processes into account and base their calculations of total cloud condensate that is liquid

Table 1. Cloud Phase Partitioning Schemes by Temperature in Various Climate Models[c]

GCM	Type	T_{min},°C	T_{max},°C	n	Reference
C20	[a]	−20	0	1	This study
C40	[a]	−40	0	1	This study
SNU	[a]	−15	0	1	*Lee et al.* [2001]
S90	[a]	−15	0	2	*Smith* [1990]
LMD	[a]	−15	0	6	*Doutriaux-Boucher and Quaas* [2004]
ERA40	[a]	−23	0	2	*Weidle and Wernli* [2008]
MIROC low	[a]	−15	0		*Le Treut and Li* [1991]
MIROC high	[a]	−25	−5		*Le Treut and Li* [1991]
UIUC	[a]	−30	0		*Sundqvist* [1988]
CAM3	[a]	−40	−10	1	*Collins et al.* [2004]
CAM5	[a]	−35	−5	1	*Song et al.* [2012]
GISS, Land	[b]	−40	−10	2	*Del Genio et al.* [1996]
GISS, Ocean	[b]	−40	−4	2	*Del Genio et al.* [1996]

[a]Cloud liquid fraction $= \left(\frac{T-T_{min}}{T_{max}-T_{min}}\right)^n$, for $T_{min} \le T \le T_{max}$.

[b]Cloud liquid fraction $= \exp\left[-\left(\frac{T_{max}-T}{15}\right)^n\right]$, for $T_{min} \le T \le T_{max}$.

[c]The C20 and C40 are the schemes used in this study. More details can be also found in *Tsushima et al.* [2006] and *Klein et al.* [2009].

solely on temperature [*Doutriaux-Boucher and Quaas,* 2004; *Weidle and Wernli,* 2008; *Klein et al.,* 2009; *Choi et al.,* 2010a, 2010b; *Hu et al.,* 2010]. However, an increasing number of state-of-the-art models are implementing parameterizations of ice nucleation that allow cloud phase to vary at a given temperature [*Storelvmo et al.,* 2008; *Gettelman et al.,* 2012]. The parameterizations are largely based on previous empirical and theoretical studies suggesting that the liquid cloud fraction should depend not only on temperature alone but also on the presence of ice-nucleating aerosols (IN). It is a well-established fact that the liquid fraction increases with increasing temperature and decreases with ice nuclei concentration at temperatures above −40°C [*Mason,* 1957; *Pruppacher and Klett,* 1997].

An adjustment of the partitioning scheme of liquid and ice makes cloud phase composition respond differently to temperature change and therefore alters cloud feedbacks, especially those associated with shortwave (SW) radiation. This is potentially critical because SW cloud feedbacks are known to be one of the main underlying factors contributing to uncertainties in climate sensitivity [*Webb et al.,* 2006; *Meehl et al.,* 2007]. Indeed, the strength of SW cloud feedbacks remains unclear since it is very difficult to estimate from observations [*Lindzen and Choi,* 2009, 2011]. More importantly, in addition to cloud feedbacks, changes in other major climate feedbacks such as surface albedo and water vapour feedbacks should also be investigated in association with changes in cloud phase composition because these feedback mechanisms are inherently coupled. Despite this, most cloud phase studies have been dedicated to determining the changes in cloud radiative effects or cloud feedbacks alone [*Li and Le Treut,* 1992; *Senior and Mitchell,* 1993; *Ho et al.,* 1998].

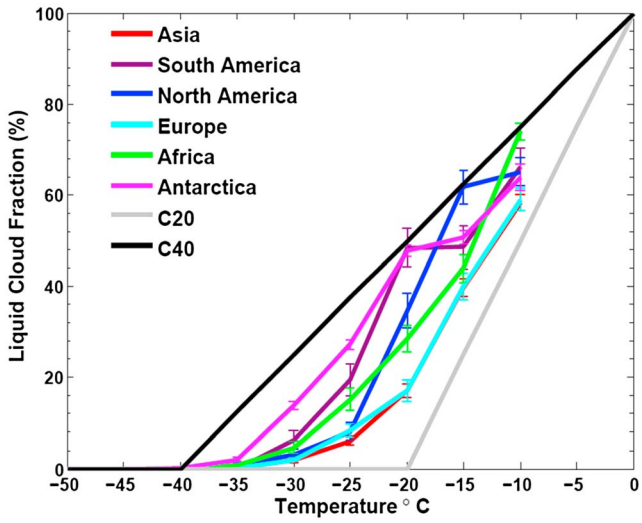

Figure 1. Cloud phase functions, C20 (grey line) and C40 (black line), used in this study. Coloured lines represent regional observations from CALIOP; CALIOP version 3 VFM products were used for December 2007 to June 2012. Following the method of *Choi et al.* [2010a], the liquid cloud fraction was calculated as the ratio of the number of liquid-phase footprints to the number of the total (liquid- and ice-phase) footprints. Note that ice includes both randomly oriented ice and horizontally oriented ice in the data.

Table 2. Experimental Designs for the Present-Day and Increased CO_2 for C20 and C40 cloud Phase Partitioning Functions[a]

Name	Range of Temperature for Mixed Cloud	CO_2 (ppmv)	Solar Constant (W m^{-2})
P_C20_O	[0, −20]	355	1367
P_C20	[0, −20]	355	1346
P_C40	[0, −40]	355	1367
D_C20	[0, −20]	710	1346
D_C40	[0, −40]	710	1367

[a]The present-day concentration of CO_2 is 355 ppmv, and the doubled value is 710 ppmv. All simulations were run at spectral resolution T42, corresponding approximately 2.875° × 2.875°.

To investigate the dependence of major climate feedbacks on cloud phase composition, we simulated the equilibrium temperature changes due to doubling of the concentration of atmospheric CO_2 for different temperature-dependent cloud phase functions. This study uses the National Center for Atmospheric Research (NCAR) Community Atmospheric Model Version 3.0 (CAM3) coupled to the Community Land Model Version 3.0 (CLM3) and a slab ocean model (SOM).

2. Methodology

2.1. Model Description

The atmospheric model used in this study, CAM3, has a horizontal spectral resolution of T42 (corresponding to approximately 2.875° × 2.875°) and 26 vertical levels in the hybrid-sigma coordinate scheme. Details of major physical parameterizations in CAM3 associated with cloud and radiation processes are documented in *Collins et al.* [2004]. Note that compared to other models participating in the third phase of the Coupled Model Intercomparison Project (CMIP3), CAM3 has a midrange equilibrium climate sensitivity of 2.7°C for a doubling of CO_2 [*Meehl et al.,* 2007]. Land surface processes are represented by CLM3 [*Oleson et al.,* 2004], while the SOM and thermodynamic sea ice model calculate the exchange of surface fluxes over ocean and sea ice, respectively. Heat and momentum fluxes are exchanged between CAM3, CLM3, and SOM through a flux coupler. When a SOM is used to simulate equilibrium climate, the mixed-layer depths and ocean heat transport are prescribed from climatological observations and simulations from CAM3, respectively. In the case of CAM3, the equilibrium climate sensitivity derived from simulations with the SOM is fairly similar to that produced by the model version with full-depth ocean dynamics [*Danabasoglu and Gent,* 2009].

All model results presented in this study are based on the assumption of a single ice crystal habit in all ice-containing clouds [*Ebert and Curry,* 1992]. We note that a more realistic representation of the variety of ice crystal habits and their associated optical properties in the model could potentially influence our results [*Liou,* 2002].

2.2. Model Experiments With Different Cloud Phase Functions

To test the dependence of climate sensitivity on cloud phase partitioning, we adopted two different cloud phase functions denoted by C20 and C40. The formulas of the two functions are given in Table 1. Both

Table 3. The Global, Tropical, and Extratropical Averages of Climate Variables for P_C20_O, P_C20, and P_C40 Experiments[a]

		P_C20_O	P_C20	P_C40	P_C20_O Minus P_C20	P_C20_O Minus P_C40	P_C20 Minus P_C40
Surface temperature (K)	Global	291.31	289.63	289.57	1.68	1.74	0.06
	Tropics	300.64	299.10	299.41	1.54	1.23	−0.31
	Extratropics	281.63	279.80	279.34	1.83	2.29	0.46
Vertically integrated cloud fraction (%)	Global	60.87	60.34	61.26	0.53	−0.39	−0.92
	Tropics	57.81	56.97	58.34	0.84	−0.53	−1.37
	Extratropics	64.05	63.83	64.30	0.22	−0.25	−0.47
Precipitation (mm/month)	Global	92.54	88.71	87.10	3.83	5.44	1.61
	Tropics	111.43	107.91	106.63	3.52	4.80	1.28
	Extratropics	72.92	68.75	66.81	4.17	6.11	1.94
Net downward solar flux at TOA (W m^{-2})	Global	243.59	240.62	236.93	2.93	6.66	3.69
Net downward solar flux at surface (W m^{-2})	Global	166.82	166.56	161.28	0.26	5.54	5.28
SW cloud radiative forcing (W m^{-2})	Global	−47.65	−45.25	−53.00	−2.40	5.35	7.75
LW cloud radiative forcing (W m^{-2})	Global	26.13	25.82	29.45	0.28	−3.32	−3.63
Sea-ice thickness (m)	Extratropics	0.056	0.082	0.095	−0.026	−0.039	−0.013
Surface albedo for direct radiation	Extratropics	0.273	0.279	0.282	−0.006	−0.009	−0.003
Surface albedo for diffuse radiation	Extratropics	0.249	0.255	0.259	−0.006	−0.010	−0.004

[a]Differences between the experiments are also shown.

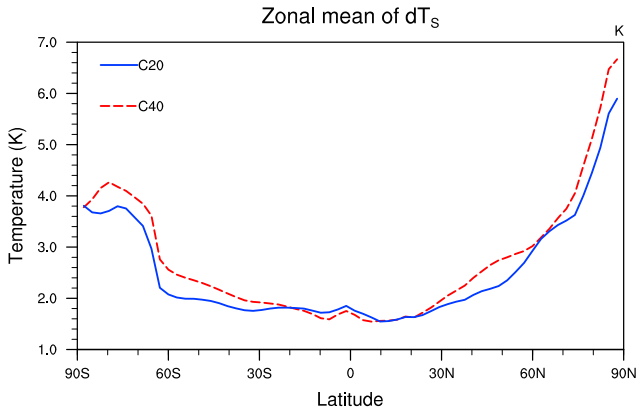

Figure 2. Zonal means of increased surface temperature to the increased CO_2 (dT_s) for clouds with C20 and C40.

functions yield a linear decrease in the liquid fraction as temperature drops below 0°C, the only difference being the temperature at which clouds will consist purely of ice: −20°C for C20 and −40°C for C40. Most cloud phase functions used in models (Table 1) as well as global measurements of liquid cloud fraction from NASA's spaceborne lidar, CALIOP (Figure 1), also fall in between C20 and C40. However, whereas the global liquid cloud fractions from other satellite observations [*Doutriaux-Boucher and Quaas,* 2004; *Weidle and Wernli,* 2008] resemble C40 more closely, the liquid cloud fraction in the polar atmosphere is much larger than that in other regions at the same temperature, far exceeding that of C20 [*Choi et al.,* 2010b; *Hu et al.,* 2010]. Hence, it is clear from observations of liquid cloud fraction that both functions are oversimplified and that using a single cloud phase function for the entire globe may not be appropriate. Nevertheless, the area between C20 and C40 corresponds to the range of uncertainty among the current climate models [*Tsushima et al.,* 2006; *Klein et al.*, 2009; *Choi et al.,* 2010b; *Hu et al.,* 2010]. Note that the default CAM3 cloud phase function is more similar to C40 (Table 1). In the actual atmosphere, the cloud phase function is controlled primarily by the amount of ice-nucleating aerosols lofted to cold cloud layers [*Choi et al.,* 2010a].

To calculate the equilibrium climate sensitivity for each cloud phase function, five 50year equilibrium simulations were performed—three for the present-day concentration of CO_2 (P_C20_O, P_C20, and P_C40), and two for the doubled concentration of CO_2 (D_C20 and D_C40), using CAM3 with SOM (Table 2). The difference between P_C20_O and P_C20 is the solar constant; the standard solar constant of 1367 W m^{-2} is used for P_C20_O, while the solar constant is reduced to 1346 W m^{-2} for P_C20. As we will discuss in

Table 4. Global, Tropical, and Extratropical Averages of Temperature Change and Feedback Estimates in Response to Increased CO_2[a]

	Variables	Unit	Globe	Tropics	Extra Tropics	Comment
a	dT_s(C20)	K	2.07	1.72	2.42	CAM3 output
	dT_s(C40)	K	2.22	1.71	2.75	CAM3 output
	dT_s'	K	−0.15	0.01	−0.33	C20−C40
b	λ(C20)	$Wm^{-2}K^{-1}$	−1.62	−1.95	−1.38	Calculated from a
	λ(C40)	$Wm^{-2}K^{-1}$	−1.51	−1.96	−1.22	Calculated from a
	$\lambda\alpha'$	$Wm^{-2}K^{-1}$	−0.11	0.01	−0.16	C20−C40
c	λ_0(C20)	$Wm^{-2}K^{-1}$	−3.41	−3.47	−3.34	Planck
	λ_0(C40)	$Wm^{-2}K^{-1}$	−3.37	−3.20	−3.54	
	λ_0'	$Wm^{-2}K^{-1}$	−0.04	−0.27	0.20	C20−C40
d	λ_L(C20)	$Wm^{-2}K^{-1}$	−0.90	−1.67	−0.10	Lapse rate
	λ_L(C40)	$Wm^{-2}K^{-1}$	−0.85	−1.66	−0.01	
	λ_L'	$Wm^{-2}K^{-1}$	−0.05	−0.01	−0.09	C20−C40
e	λ_w(C20)	$Wm^{-2}K^{-1}$	1.43	2.47	0.35	Water vapor
	λ_w(C40)	$Wm^{-2}K^{-1}$	1.41	2.43	0.35	
	λ_w'	$Wm^{-2}K^{-1}$	0.02	0.03	0	C20−C40
f	λ_α(C20)	$Wm^{-2}K^{-1}$	0.20	0.01	0.39	Surface albedo
	λ_α(C40)	$Wm^{-2}K^{-1}$	0.23	0.01	0.46	
	λ_α'	$Wm^{-2}K^{-1}$	−0.03	0	−0.07	C20−C40
g	λ_C(C20)	$Wm^{-2}K^{-1}$	1.06	0.71	1.32	Cloud
	λ_C(C40)	$Wm^{-2}K^{-1}$	1.07	0.46	1.52	
	λ_C'	$Wm^{-2}K^{-1}$	−0.01	0.25	−0.20	C20−C40
h	λ'/λ(C40)	%	7.28	0.51	13.11	Proportion

[a]The tropics (30°S–30°N) and the extratropics are separated. The prime indicates the deviation of the value from C40 (i.e., C20 minus C40).

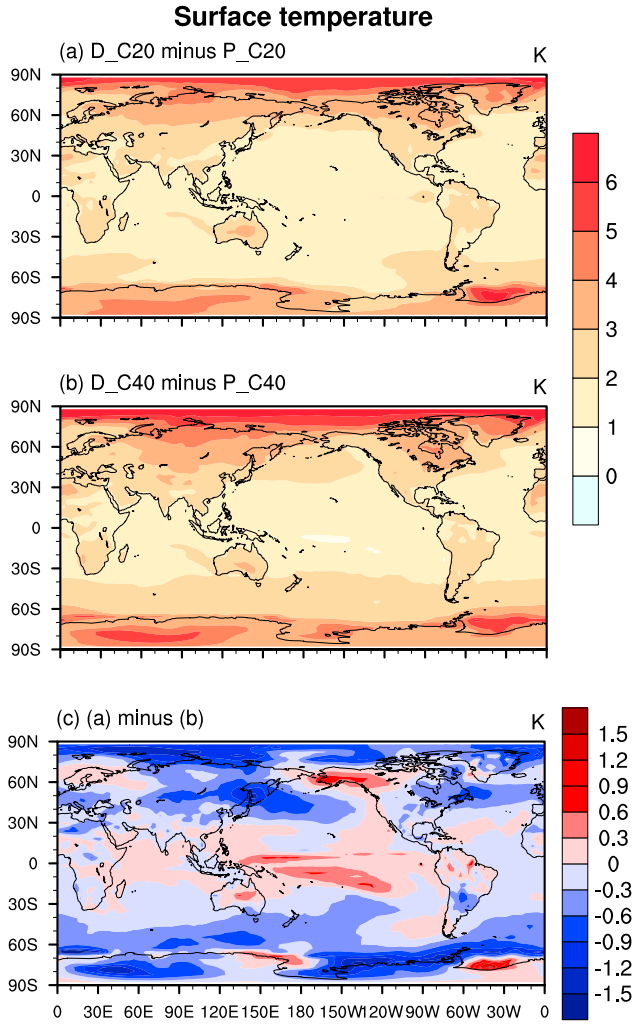

Figure 3. (a and b) Spatial distribution of climate sensitivity in response to increased CO_2 (dT_s) and (c) the difference.

section 2.2, the purpose of adjusting the solar constant in P_C20 is to minimize the difference between its modeled climate state and that of P_C40, which thereby isolates the influence of cloud phase function. Thus, we will mainly use P_C20, instead of P_C20_O. D_C20 minus P_C20 and D_C40 minus P_C40 represent the effects of elevated CO_2 concentration for the C20 and C40 functions, respectively. In addition, the different climate response to doubled CO_2 concentration between C20 and C40 can be represented by (D_C20 minus P_C20) minus (D_C40 minus P_C40). We analyzed the equilibrated climatology of the last 30 model years.

Table 3 summarizes the climate states of the P_C20_O, P_C20, and P_C40 experiments. The simulated global (extratropical) mean temperature for P_C20_O was much higher than that for P_C40 by ~1.74 K (2.29 K). This result illustrates the strength of the impact of cloud phase function on simulated climate state. The warmer climate for P_C20_O relative to P_C40 can be explained by the fact that optically thinner clouds allow more SW radiation to reach the surface, which consequently lowers surface albedo in the extratropics (by 0.9 and 1.0% for direct and diffuse radiation, respectively). Note that at fixed total water content, a liquid cloud is more reflective than an ice cloud, since ice crystals are relatively fewer and larger than liquid water droplets. By the same token, an ice cloud will precipitate more quickly and efficiently than a liquid cloud. Thus, converting a liquid cloud to an ice cloud implies a replacement of many small water droplets with few large ice crystals, which would reduce the lifetime and reflectivity of the cloud and increase precipitation (P_C20_O minus P_C40 in Table 3). As a consequence, the net global mean downward SW radiation for P_C20_O exceeds that of P_C40 by 6.66 and 5.54 W m^{-2} at the top of the atmosphere (TOA) and surface, respectively. In order to balance the additional absorbed SW radiation, the surface temperature in P_C20_O must be higher than that of P_C40. The resulting change in surface temperature may then induce other climate feedbacks.

To allow for a fair comparison in which the differences in climate feedbacks between the two experiments are solely due to the different cloud phase functions, the global mean temperatures of P_C20 and P_C40 were equalized by adjusting the solar constant. While it is not clear whether adjusting factors other than the solar constant, for example, Q flux that represents seasonal deep water exchange and horizontal ocean heat transport [*Collins et al.,* 2004] is more appropriate for this study, the advantage of adjusting the solar constant is that it avoids the issue of directly perturbing atmosphere and ocean coupling, which is intricately tied to climate sensitivity. We see in Table 3 that reduction of the solar constant (in P_C20) leads to lower surface temperature, fewer tropical clouds, less precipitation, less downward SW flux (mainly due to reduction of incident solar radiation), weaker SW cloud forcing, thicker sea ice, and higher surface albedo (see P_C20_O minus P_C20).

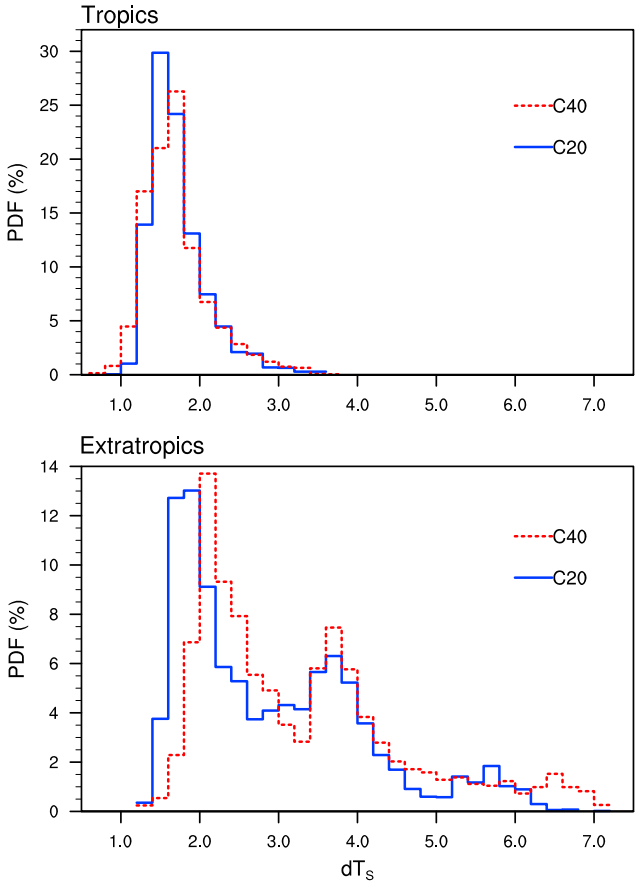

Figure 4. Probability density function of climate sensitivity to the increased CO_2 (dT_s) for a 2.8°-grid domain for clouds with C20 and C40. Forty bins of size 0.2 K are used. (a) The tropics (30°S–30°N) and (b) the extratropics (30°S–90°S and 30°N–90°N). The total number of grid points is 2816 for the tropics and 5376 for the extratropics. The probability is calculated as the percentage of total grid points in each bin.

All of these changes seem to be physically consistent with each another, and with the results of *Boer et al.* [2005], who also changed the solar constant. We note that the change in LW cloud forcing is fairly small.

Finally, Table 3 shows that reduction of the solar constant greatly reduces the difference between the two present-day climates of P_C20 and P_C40 in many important aspects such as the global-mean surface temperature, precipitation, net solar flux at TOA, sea-ice thickness, and surface albedo. For these properties, the differences between P_C20 and P_C40 are approximately 3−55% of the original differences between P_C20_O and P_C40. However, differences in the simulated cloud fraction and SW cloud radiative forcing increase slightly.

2.3. Calculation of Climate Feedbacks

Climate feedbacks are defined in terms of changes in global (or regional) mean surface temperature ($\overline{T}_s$), and changes in radiative flux at the top of the atmosphere (R). For each cloud phase function, the equilibrium surface temperatures, $\overline{T}_s$, are calculated for present-day and doubled CO_2 concentrations. The temperature difference, $d\overline{T}_s$, between the doubled and the present-day CO_2 concentrations (i.e., D_C20 minus P_C20 for C20, and D_C40 minus P_C40 for C40) thus yields the equilibrium climate sensitivity for an imposed radiative forcing due to the doubling of CO_2 (3.35 W m^{-2} from the calculation based on the initial change in net downward radiative flux at TOA in the present model) [*Gregory et al.*, 2004]. We define the total climate feedback parameter, λ, to be the total derivative $dR/d\overline{T}_s$ that can be expanded using the chain rule:

$$\lambda = \frac{dR}{d\overline{T}_s} = \sum_i \frac{\partial R}{\partial x_i}\frac{dx_i}{d\overline{T}_s} \tag{1}$$

where the last term in equation (1) indicates that the change in flux is due to not only changes in $\overline{T}_s$ but also the various auxiliary variables x_i (e.g., lapse rate (L), cloud (C), water vapor (w), and albedo (α)) that are influenced by $\overline{T}_s$. Equation (1) can be equivalently rewritten as

$$\lambda = \lambda_0 + \lambda_L + \lambda_C + \lambda_w + \lambda_\alpha \tag{2}$$

where

$$\lambda_0 = \frac{\partial R}{\partial T_s}\frac{dT_s}{d\overline{T}_s} + \frac{\partial R}{\partial \overline{T}}\frac{d\overline{T}_s}{d\overline{T}_s}, \tag{3a}$$

$$\lambda_L = \frac{\partial R}{\partial T}\frac{dT}{d\overline{T}_s} - \frac{\partial R}{\partial \overline{T}}\frac{d\overline{T}_s}{d\overline{T}_s}, \tag{3b}$$

$$\lambda_i = \frac{\partial R}{\partial x_i}\frac{dx_i}{d\overline{T}_s} \qquad \text{for } i = C, w, \alpha \tag{3c}$$

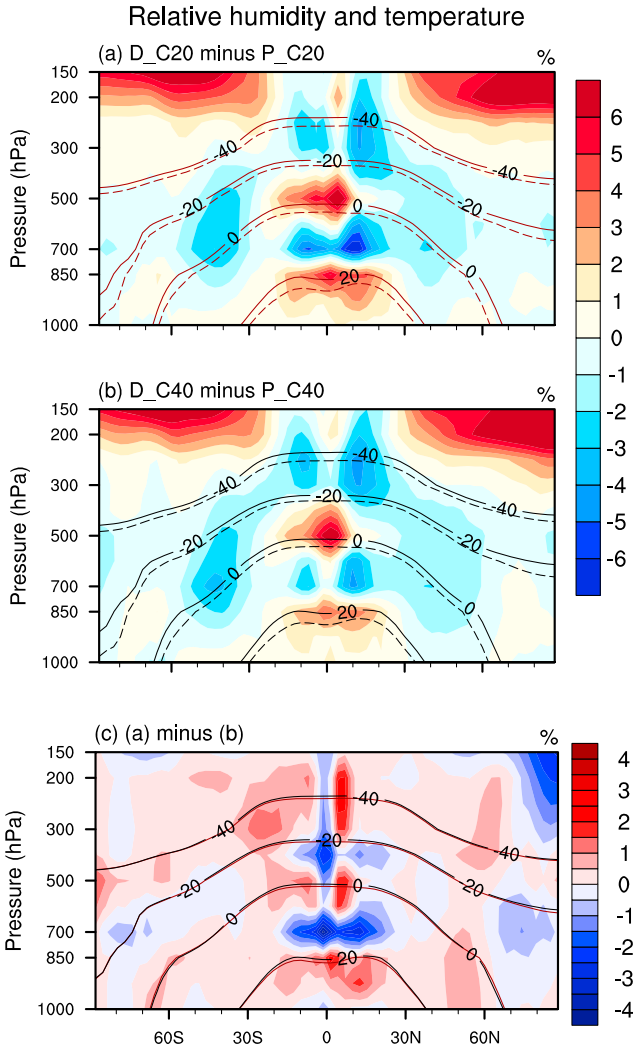

Figure 5. Zonal mean of changes in relative humidity in response to increased CO_2 for clouds with C20 (a) and C40 (b). (c) The difference (C20 minus C40). The solid lines indicate zonally averaged temperatures for D_C20 (purple) and D_C40 (black); the dashed lines indicate zonally averaged temperatures for P_C20 (purple) and P_C40 (black).

are the climate feedback parameters associated with the atmospheric variable x_i (in units of W m^{-2} K^{-1}). The dx_i and $d\overline{T}_s$ are the differences in x_i and global mean surface temperatures between the present-day and the doubled CO_2 climate simulations, respectively. The partial derivatives $\partial R/\partial x_i$ are called the radiative feedback kernels. This "radiative kernel method" developed by *Soden and Held* [2006] has been widely used to compute individual feedbacks in previous studies [see, e.g., *Shell et al.,* 2008; *Jonko et al.,* 2012]. In this study, the CAM radiative kernels are used [*Shell et al.,* 2008]. The Planck response is represented as λ_0, i.e., the negative feedback associated with the temperature dependence of thermal emission. It is calculated assuming uniform temperature change throughout the troposphere in the absence of changes in lapse rate. It is expressed as the sum of the surface temperature kernel and the atmospheric temperature (T) kernel at every level below the tropopause, both of which are multiplied by dT_s and normalized by $d\overline{T}_s$ (equation (3a)). The tropopause is defined to be at 100 hPa at the equator and linearly increases with latitude until it reaches 300 hPa at the poles [*Soden and Held,* 2006; *Jonko et al.,* 2012]. The lapse rate feedback (λ_L) is computed as the product of the T kernel and the lapse rate change ($dT - dT_s$), normalized by $d\overline{T}_s$ (equation (3b)). The sum $\lambda_0 + \lambda_L$ is referred to as the "temperature feedback" (λ_T).

The water vapor and albedo feedbacks (λ_w and λ_α) are calculated by multiplying the water vapor and albedo kernels by differences in the natural log of specific humidity and surface albedo between the doubled CO_2 and present climate simulations, respectively (equations (3c) and (3d)). Due to nonlinearities in the calculation of the kernel arising from complicated vertical overlap of clouds, λ_C is computed as the residual difference between λ and other feedback parameters in equation (2). However, we note that this residual method of calculation for cloud feedback is a potential source of error in our calculations since other feedbacks may be dependent on cloud feedbacks themselves. Each λ_i is a function of latitude, longitude, and altitude (except for surface albedo feedback). Global feedback parameters are calculated by integrating from the surface to the tropopause and averaging globally.

The change in the climate feedback parameters due to the cloud phase change from C40 to C20 is then

$$\lambda' = \lambda'_0 + \lambda'_L + \lambda'_C + \lambda'_w + \lambda'_\alpha \tag{4}$$

where the primes indicate deviations from the feedback value of C40 (i.e., C20 minus C40).

The climate feedback parameters represented in equations (1) to (4) are calculated for the tropics and extratropics in this study. However, it should be borne in mind that the feedback parameter for a given region cannot be directly compared to that for the globe or that for any other region.

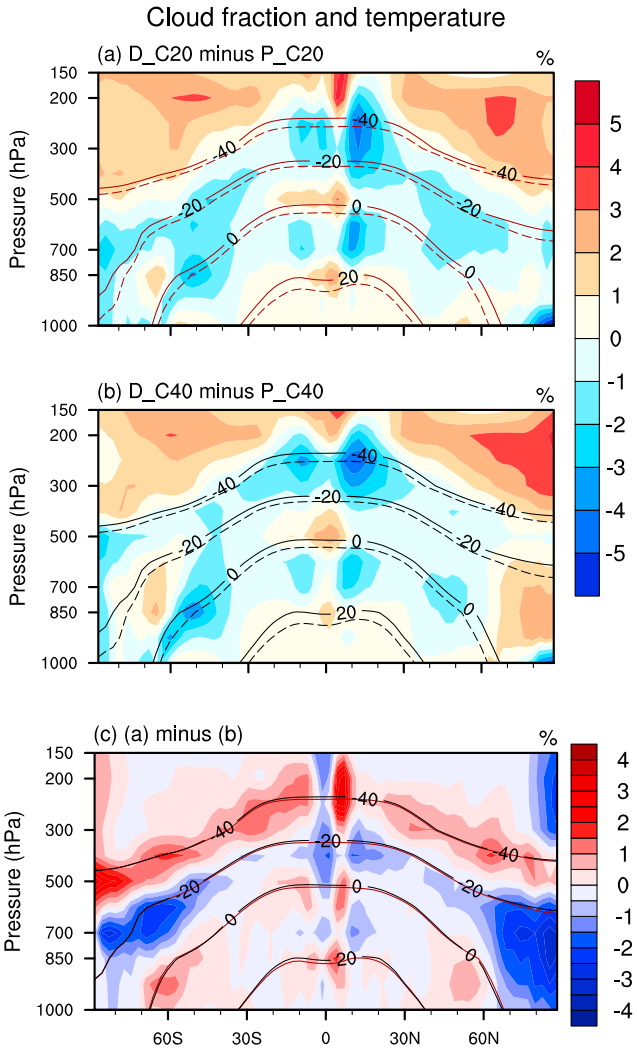

Figure 6. The same as Figure 5, but for cloud fraction.

3. The Influence of Cloud Phase Composition on Climate Feedbacks

The two cloud phase partitioning schemes, C20 and C40 (Figure 1), can influence cloud feedbacks in two opposing ways. In the C20 scheme, clouds are purely composed of ice particles at temperatures between −40°C and −20°C. Thus, one would expect a stronger mixed-phase cloud response for C40 than for C20 at temperatures between −40°C and −20°C. However, the stronger mixed-phase cloud response for C40 may be counteracted by the more rapid change in liquid cloud fraction at temperatures warmer than −20°C in the C20 scheme, where the liquid fraction decreases more rapidly with decreasing temperature. At temperatures warmer than −20°C, one would expect C20 to yield a stronger cloud response induced by the CO_2 warming. As a consequence, these two opposing effects might compete in determining the total cloud feedback. Since the cloud feedback is also strongly coupled with other climate feedback processes, substantial changes in the magnitude of various climate feedbacks are expected. In order to investigate how climate feedbacks are altered, we shall begin with discussing the equilibrium climate sensitivity, which is a consequence of climate feedbacks induced by warming.

Figure 2 shows the zonal mean surface temperature in response to increased CO_2 concentration (dT_s), simulated for C20 (blue solid line) and C40 (red dashed line). $d\overline{T}_s$ is generally larger at higher latitudes, reaching a maximum of ~7 K in the arctic. At most latitudes, dT_s for C20 is lower than that for C40, with the exception of the equatorial region. In the extratropics, the dT_s difference between C20 and C40 appears to be statistically significant, as compared to the standard deviation of only 0.1 K of dT_s resulting from interannual variability [*Danabasoglu and Gent*, 2009]. As we will show later with our calculations of individual feedbacks (Table 4), this difference is largely caused by changes in the surface albedo and cloud feedbacks. In the tropics, however, changes in surface albedo feedback between C20 and C40 are negligible, because the tropical surface albedo feedback is close to zero in both simulations.

Figure 3 expands the zonally averaged dT_s in Figure 2 to a latitude-longitude domain. dT_s for C20 (Figure 3a) and C40 (Figure 3b) and the difference (C20 minus C40, Figure 3c) are displayed. As expected, the temperature response, dT_s is larger over the continents and lower over the ocean for a given latitude (Figures 3a and 3b). dT_s is generally larger in C20 than in C40 in the tropics (red shade in Figure 3c), particularly in the tropical Pacific. On the contrary, dT_s is lower for C20 than for C40 (blue shading in Figure 3c) in the extratropics.

To characterize the frequency distribution of dT_s, the probability density functions (PDFs) of grid point values of dT_s for C20 and C40 are shown in Figure 4. In the tropics, the PDF of dT_s for C20 (blue solid line) has a similar distribution to that for C40 (red dotted line); only slight differences between the PDFs of C40 and C20 exist.

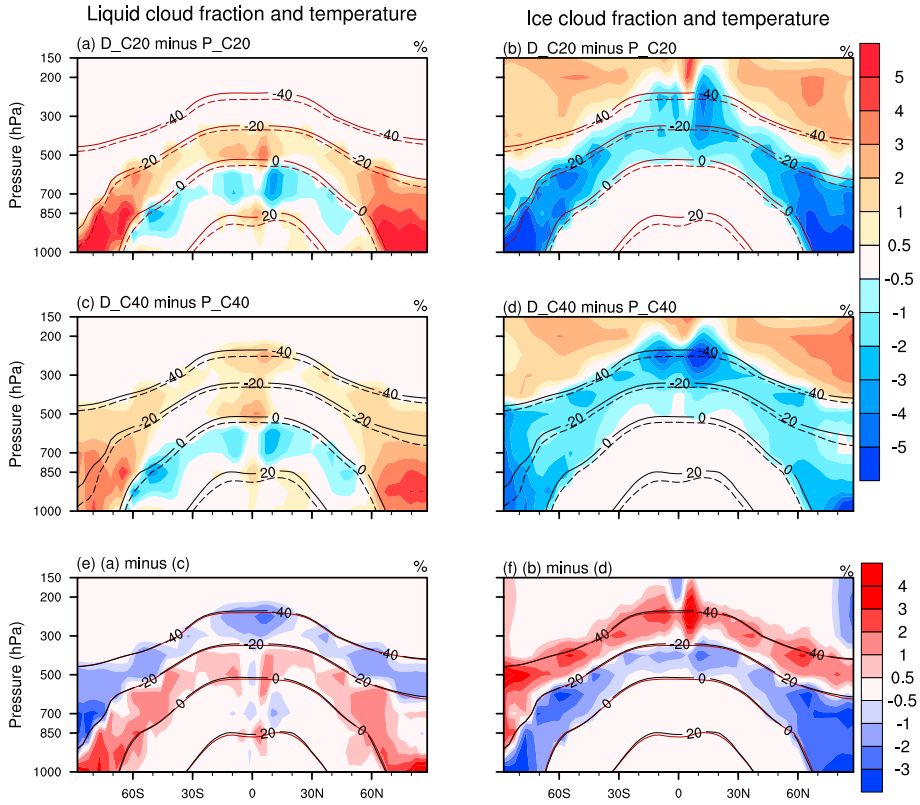

Figure 7. The zonal mean of the liquid and ice cloud fraction profile in response to the increased CO_2 for clouds with (a and b) C20 and (c and d) C40. The difference (C20 minus C40) is shown for (e) liquid and (f) ice cloud fraction, respectively. The solid lines indicate zonally averaged temperatures for D_C20 (purple) and D_C40 (black); the dashed lines indicate zonally averaged temperatures for P_C20 (purple) and P_C40 (black).

However, analysis of the extratropics tells a different story. There are three peaks in the PDFs of $d\overline{T}_s$ located at approximately 2 K, 4 K, and 6 K. The first peak is shifted to the right, to higher temperatures for C40. The probability that $d\overline{T}_s > 4$K is generally larger in C40 than in C20, which reflects the stronger surface warming in C40 in the northern hemisphere middle and high latitudes (see Figure 3). In summary, Figures 2–4 all consistently show that $d\overline{T}_s$ for C20 is lower than that for C40 in the extratropics (especially over continents), while the difference is not as pronounced in the equatorial regions.

The feedback strengths corresponding to $d\overline{T}_s$ for the globe, tropics, and extratropics were calculated from equations (1) to (4) and are shown in Table 4. The change in climate feedbacks (C20 minus C40) accounts for ~7.28% of the global feedback for C40 and is dominated by the change in the extratropics (13.11%, Table 4h). However, the largest change in individual feedback strength occurs in tropical clouds (0.25 W m^{-2} K^{-1}). This change in the sum of tropical cloud feedbacks is largely compensated by the change in Planck feedback (−0.27 W m^{-2} K^{-1}) (Table 4c, g). Thus, although the net change in the total climate feedback is very small in the tropics (0.51% of the total) (Table 4h), it is clear that this is a result of compensation between larger changes in individual feedbacks. The extratropical feedback change is associated with changes in all but the water vapour feedback (Table 4c to g).

The changes in the various feedback mechanisms can be understood by examining the vertical profiles of responses to the doubled CO_2 concentration. When the atmospheric CO_2 concentration increases, an increase in surface temperature follows, causing the temperature profile to rapidly adjust to a new radiative-convective equilibrium [*Lindzen et al.,* 1982]. This is clearly shown in Figure 5 (solid line for present-day climate and dashed line for doubled CO_2 climate). Regions in the atmosphere with temperatures between the −40°C and 0°C are regions in which the composition of mixed-phase clouds is affected by temperature changes.

These temperature adjustments can change relative humidity (RH), especially in the upper troposphere and lower stratosphere in the extratropics (colored contours in Figure 5). However, the upper level changes have a

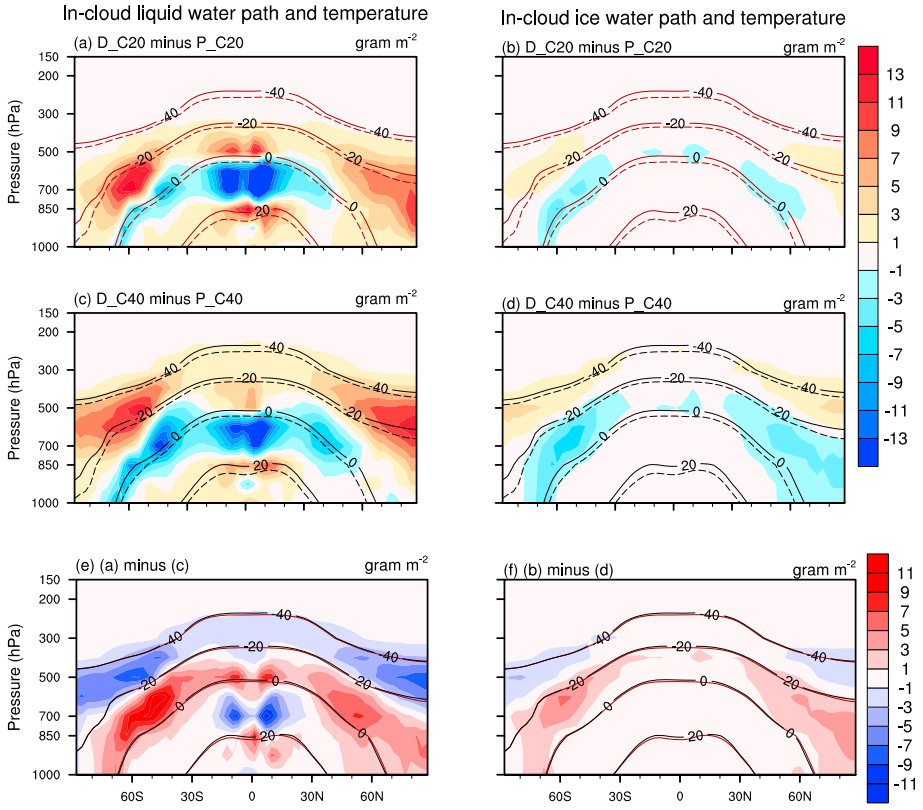

Figure 8. The same as Figure 7, but for in-cloud liquid water path and ice water path.

negligible effect on feedback because the concentration of water vapor at that level is low. In the mid- and lower troposphere, most of the change in RH is largest in the tropics. Interestingly, the pattern of the tropical tropopause RH response is complex and shows large changes of opposite signs for different heights (Figures 5a and 5b), likely due to changes in shallow and deep convection (Figure 6). Despite this complicated vertical response of RH, the vertically integrated specific humidity in the tropics in response to warming for C20 and C40 are nearly equal. This explains why the water vapor feedback was virtually unchanged (Table 4e).

The cloud fraction response to doubled CO_2 concentration (hereafter dA_c) is shown in Figure 6. dA_c for mixed-phase clouds (between −40°C and 0°C) is generally negative except at a few altitudes in the tropics (Figures 6a and 6b). In both C20 and C40, there is a strong reduction of tropical high clouds in response to doubled CO_2 concentration. These high clouds have the potential to allow more SW radiation into the tropical atmosphere, which can explain the positive tropical cloud feedback in the model (Table 4g). In contrast, there is an increase in high clouds above 300 hPa in the entire extratropics and a decrease of low clouds around 850 hPa in the midlatitudes in response to the doubled CO_2 concentration in both C20 and C40. This may act to increase trapping of LW radiation and penetration of SW radiation to the surface, which explains the positive extratropical cloud feedback in the model (Table 4g). As we will show in Figure 10, the SW responses dominate the longwave (LW) responses in general.

The relationship between cloud feedback and cloud phase function can be inferred from (Figure 6c). dA_c(C20) minus dA_c(C40) for ice-phase clouds (around −40°C level) is positive. In contrast, dA_c(C20) minus dA_c(C40) for cold mixed-phase clouds (around −20°C level) is negative. The contributions of liquid (a, c, e) and ice cloud fractions (b, d, f) to the total cloud fractions (Figure 6) are displayed in Figure 7. We see that the response of ice cloud fraction to doubling of CO_2 (Figures 7b and 7d) is more similar to the total cloud fraction in Figure 6 than the water cloud fraction (Figures 7a and 7c). Between −40°C and 0°C, the sign of the change is the opposite between liquid- and ice-phase cloud fractions (Figure 7e versus Figure 7f). Overall, it can be said that the pattern of the total cloud fraction change is consistent with the changes in liquid-phase cloud fraction above 0°C and ice-phase cloud fraction below 0°C. Note that all of the above effects strongly influence cloud

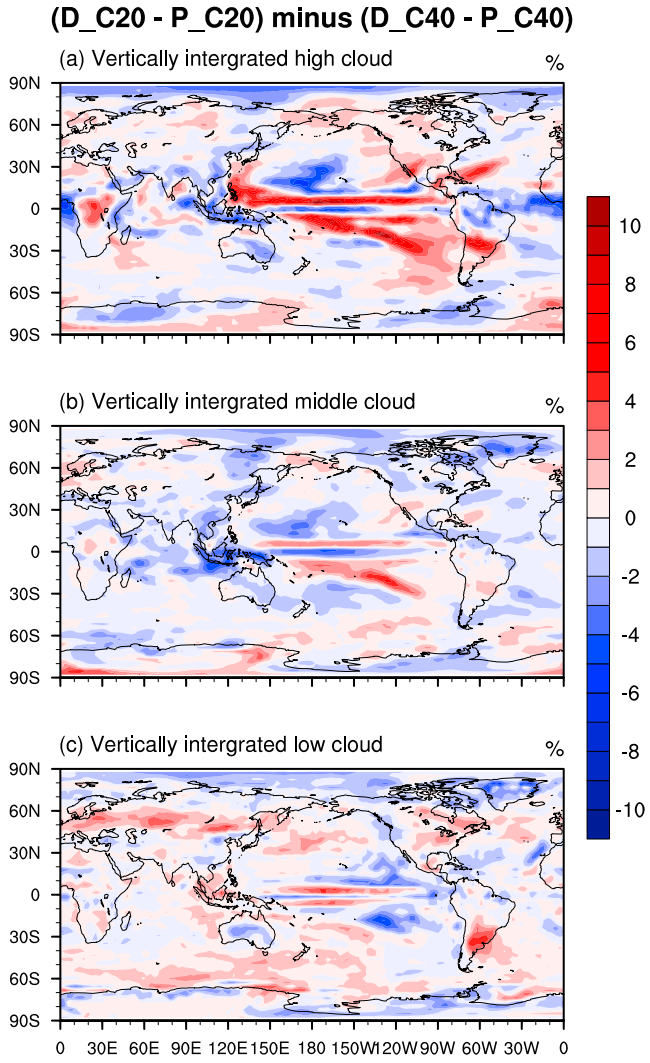

Figure 9. The difference (C20 minus C40) in the regional distribution of (a) high clouds (top pressure < 400 hPa), (b) midlevel clouds (700 hPa ≤ top pressure < 400 hPa), and (c) low clouds (top pressure ≥ 700 hPa) in response to the increased CO_2.

feedback change. While the change in cloud feedback strength is not readily identified in Figures 6 and 7, the results in Table 4g indicate that the tropical cloud feedback strengthens in C20, while the extratropical cloud feedback weakens relative to C40.

The responses of the in-cloud liquid and ice water paths (LWP and IWP) to the changes in cloud phase composition are other factors that can alter cloud feedback because LWP and IWP strongly influence the emissivity and reflectivity of mixed-phase clouds. The LWP and IWP are calculated as grid-mean cloud water paths (CWP) weighted by liquid- and ice-phase cloud fractions, respectively; $LWP = CWP(1 - A_i) / A_c$ and $IWP = CWP \cdot A_i / A_c$, where A_i is the ice cloud fraction. In general, the model-simulated LWP changes much more than IWP (Figure 8). Changes in LWP are generally positive for mixed-phase clouds (between −40°C and 0°C), while they are negative for warm clouds (between 0°C and 20°C) in response to doubled CO_2 concentration (Figures 8a and 8c). The reduction of LWP for warm clouds is consistent with the reduction of warm-cloud fraction (compare Figures 7 and 8). On the other hand, changes in IWP are positive between −40°C and −20°C and negative between −20°C and 0°C in response to doubled CO_2 concentration (Figures 8b and 8d). The ratio of LWP to IWP has an important implication. Comparing Figures 8a and 8b (or Figures 8c and 8d), an increase in LWP and a decrease in IWP are evident for mixed-phase clouds between −20°C and 0°C. This means that these clouds may become brighter and reflect more SW radiation in response to doubled CO_2 concentration. This LWP/IWP effect alone would yield a negative cloud feedback. However, Table 4g shows a positive overall cloud feedback in CAM3. This implies that the LWP/IWP effect is secondary to the cloud fraction effect in determining cloud feedback strength.

As for the difference between C20 and C40, Figure 8e shows that above (below) the −20°C isotherm, LWP increases (decreases) for C20 to a smaller extent than for C40. A similar but smaller change in IWP is also found at a slightly higher altitude (Figure 8f). These results indicate that both IWP and LWP generally covary but that a decrease in the LWP/IWP ratio in C20 relative to C40 can be expected close to the −20°C isotherm. This decrease in LWP/IWP ratio would lead to a decrease in SW cloud albedo, possibly intensifying the positive cloud feedback in the tropics (Table 4g).

Figure 9 shows the difference (C20 minus C40) in dA_c for high clouds (top pressure < 400 hPa) (a), midlevel clouds (400 hPa ≤ top pressure < 700 hPa) (b), and low clouds (top pressure ≥ 700 hPa) (c). In the global mean, the difference in dA_c between C20 and C40 is nearly zero (0.001, −0.004, and 0.001 for high, mid-level, and

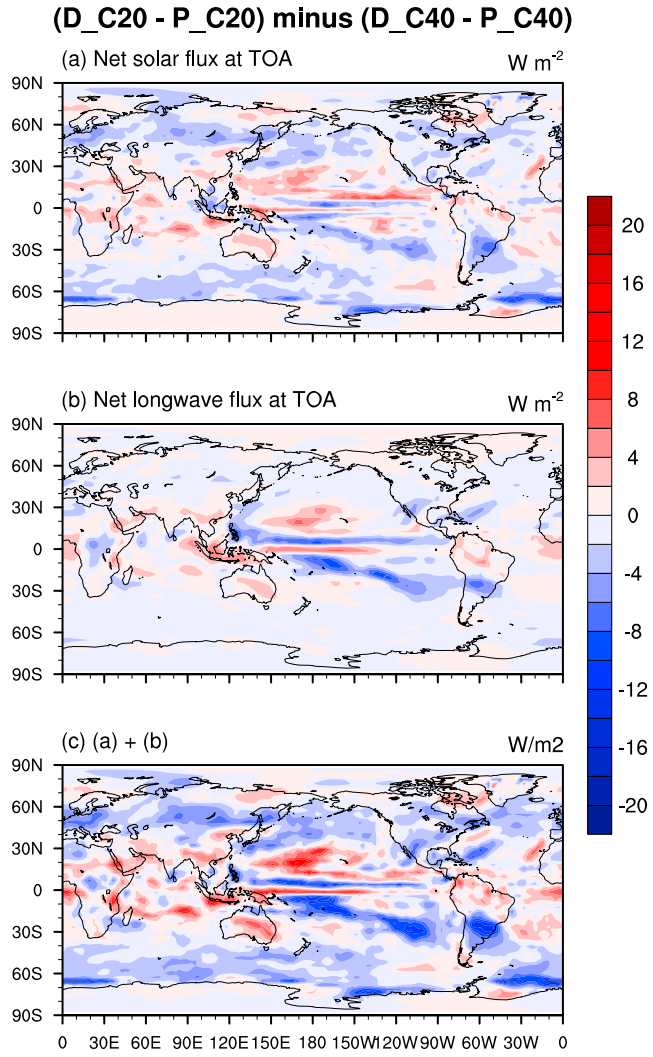

Figure 10. The difference (C20 minus C40) in the top-of-atmosphere (a) shortwave and (b) longwave radiative flux in response to increased CO_2. (c) Obtained by the sum of Figures 10a and 10b. Positive values indicate downward fluxes.

low clouds, respectively); however, strong regional variability does exist. The difference in dA_c for high clouds is more pronounced in the tropics than in the extratropics; the difference in dA_c for mid-level clouds is mostly negative; the difference in dA_c for low clouds is mostly positive over the northern hemispheric continents. The positive difference for low clouds would imply less absorbed SW radiation in the atmosphere.

Figure 10 shows the difference (C20 minus C40) in downward SW and LW radiation perturbations at the top of the atmosphere due to doubling of CO_2. As expected, the difference in SW flux is mostly negative and is anticorrelated with low cloud changes (compare Figures 9c and 10a). On the other hand, the difference in LW flux is mostly negative and is anticorrelated with the changes in mid-level clouds (compare Figures 9b and 10b). Both SW and LW fluxes (Figures 10a and 10b) exhibit a double-ITCZ type pattern along a long narrow tropical band, which is more clearly shown in the summation of SW and LW (Figure 10c). In spite of large localized flux changes of opposite sign throughout the tropics, the average turns out to be a very small difference in the net tropical feedback ($\lambda' = -0.01$ W m^{-2} K^{-1} in Table 4b). Note that this does not hold true for the extratropics, where SW fluxes exhibit more variability than longwave fluxes. In these regions, the change in cloud phase composition from C40 to C20 weakens the feedback ($\lambda' = -0.16$ W m^{-2} K^{-1} in Table 4b).

4. Discussion and Conclusions

The dependence of our results on CAM3 as our choice of model requires some discussion. CAM3 has been widely used and tested in many climate feedback studies [*Collins et al.,* 2006; *Shell et al.,* 2008; *Penner et al.,* 2009; *Cao et al.,* 2009; *Jeong et al.,* 2010]. However, estimated feedback values can be subject to specific settings of the present experiments. In particular, the estimation of cloud feedback in CAM3 can be influenced by ocean dynamics [*Jonko et al.,* 2012]. The difference in the cloud feedback of CAM3 can be as large as 0.06 W m^{-2} between simulations with a slab ocean model and a fully interactive ocean model [*Jonko et al.,* 2012] in response to doubled CO_2 concentrations. The difference is computed by separating the net cloud feedback into shortwave and longwave cloud feedbacks [*Shell et al.*, 2008; *Jonko et al.*, 2012]. This method was not applied in the present study but will be useful in future studies that focus on cloud feedbacks.

The present study has shown that climate feedbacks are highly sensitive to temperature-dependent cloud phase functions. Here, we have used two different cloud phase functions, C20 and C40, to reflect the variability of cloud phase dependence on temperature found among various models. In the C20 (C40) experiment, all liquid droplets are converted to ice crystals below −20°C (−40°C), so that both liquid and ice clouds co-exist at temperatures between 0°C and −20°C (−40°C). By adjusting the solar constant, the global annual mean temperatures in C20 and C40 were set to be similar. Doing otherwise would cause a significant mean surface temperature difference of ~1.7°C between C20 and C40, leading to different climatologies in precipitation, surface albedo, etc. between the two cloud phase partitioning schemes that would not allow for fair comparisons between C20 and C40.

Our simulations show that changing the cloud phase function from C40 to C20 alters the cloud feedback in the tropics by 0.25 W m^{-2} K^{-1} and in the extratropics by −0.20 W m^{-2} K^{-1}, the temperature feedback in the tropics by −0.28 W m^{-2} K^{-1} and in the extratropics by 0.11 W m^{-2} K^{-1}, and the albedo feedback in the extratropics by −0.07 W m^{-2} K^{-1}. Due to compensation of feedback changes, the net change in global climate feedback is 7.3% of the total feedback (−0.11 W m^{-2} K^{-1}) and is dominated by changes in the extratropics. The influence of the solar constant on feedbacks is negligible. These results suggest that adjustment of the cloud phase function affects all types of feedbacks (with the least effect on water vapor feedback). Although there are substantial differences in the individual climate feedbacks between the two cloud phase partitioning schemes, cancellation of the various feedbacks resulted in a small net change in the overall climate feedback. However, should the climate system be very sensitive to an increase in CO_2, even a small change in the net climate feedback induced by changes in the cloud phase partitioning scheme would lead to a large bias in climate prediction [*Roe and Baker,* 2007].

As revealed by satellite observations, significantly different regional and transient variations of the cloud phase function occur naturally mainly due to the role of dust aerosols [*Choi et al.,* 2010a]. A smaller liquid cloud fraction was generally observed at lower latitudes and in regions with abundant dust aerosols in cold cloud layers. In light of the complex regional and vertical distributions of liquid cloud fraction, this study implies that recent investigations with more sophisticated modeling of aerosol-cloud interactions are of vital importance for accurate simulations of climate feedbacks, and by extension, climate prediction.

Acknowledgments

This study was supported by the National Research Foundation of Korea (NRF) grant funded by the Korea government (MSIP) (2009-0083527) and the Korea Meteorological Administration Research and Development Program under grant CATER 2012–3064. The authors thank R. S. Lindzen for valuable comments. The radiative kernels for this paper are available at K. M. Shell's homepage (http://people.oregonstate.edu/~shellk/kernel.html). Kernel files: Kernels.zip. The CALIOP data are available online at the NASA Langley Atmospheric Sciences Data Center website (https://eosweb.larc.nasa.gov/order-data).

References

Boer, G. J., K. Hamilton, and W. Zhu (2005), Climate sensitivity and climate change under strong forcing, *Clim. Dyn.*, *24*, 685–700.

Bretherton, C. S., and S. Park (2009), A new moist turbulence parameterization in the Community Atmosphere Model, *J. Clim.*, *22*, 3422–3448.

Cao, L., G. Bala, K. Caldeira, R. Nemani, and G. Ban-Weiss (2009), Climate response to physiological forcing of carbon dioxide simulated by the coupled Community Atmosphere Model (CAM3.1) and Community Land Model (CLM3.0), *Geophys. Res. Lett.*, *36*, L10402, doi:10.1029/2009GL037724.

Choi, Y.-S., R. S. Lindzen, C.-H. Ho, and J. Kim (2010a), Space observations of cold-cloud phase change, *Proc. Natl. Acad. Sci. U.S.A.*, *107*, 11,211–11,216.

Choi, Y.-S., C.-H. Ho, S.-W. Kim, and R. S. Lindzen (2010b), Observational diagnosis of cloud phase in the winter Antarctic atmosphere for parameterizations in climate models, *Adv. Atmos. Sci.*, *27*, 1233–1245.

Collins, W. D., et al. (2004), *Description of the NCAR Community Atmosphere Model (CAM 3.0)*, National Center for Atmospheric Research, Boulder, Colo.

Collins, W. D., P. J. Rasch, B. A. Boville, J. J. Hack, J. R. McCaa, D. L. Williamson, B. P. Briegleb, C. M. Bitz, S.-J. Lin, and M. Zhang (2006), The Formulation and atmospheric simulation of the Community Atmosphere Model version 3 (CAM3), *J. Clim.*, *19*, 2144–2161.

Danabasoglu, G., and P. R. Gent (2009), Equilibrium climate sensitivity: Is it accurate to use a slab ocean model?, *J. Clim.*, *22*, 2,494–2,499.

Del Genio, A. D., M.-S. Yao, W. Kovari, and K. W. Lo (1996), A prognostic cloud water parameterization for global climate models, *J. Clim.*, *9*, 270–304.

Doutriaux-Boucher, M., and J. Quaas (2004), Evaluation of cloud thermodynamic phase parameterizations in the LMDZ GCM by using POLDER satellite data, *Geophys. Res. Lett.*, *31*, L06126, doi:10.1029/2003GL019095.

Ebert, E. E., and J. A. Curry (1992), A parameterization of ice cloud optical properties for climate models, *J. Geophys. Res.*, *97*, 3831–3836.

Gettelman, A., X. Liu, D. Barahona, U. Lohmann, and C. Chen (2012), Climate impacts of ice nucleation, *J. Geophys. Res.*, *117*, D20201, doi:10.1029/2012JD017950.

Gregory, J. M., W. J. Ingram, M. A. Palmer, G. S. Jones, P. A. Stott, R. B. Thorpe, J. A. Lowe, T. C. Johns, and K. D. Williams (2004), A new method for diagnosing radiative forcing and climate sensitivity, *Geophys. Res. Lett.*, *31*, L03205, doi:10.1029/2003GL018747.

Ho, C.-H., M.-D. Chou, M. Suarez, and K.-M. Lau (1998), Effect of ice cloud on GCM climate simulations, *Geophys. Res. Lett.*, *25*, 71–74.

Hu, Y., S. Rodier, K. Xu, W. Sun, J. Huang, B. Lin, P. Zhai, and D. Josset (2010), Occurrence, liquid water content, and fraction of supercooled water clouds from combined CALIOP/IIR/MODIS measurements, *J. Geophys. Res.*, *115*, D00H34, doi:10.1029/2009JD012384.

Intergovernmental Panel on Climate Change (2007), *Climate Change 2007: The Physical Science Basis. Contribution of Working Group I to the Fourth Assessment Report of the Intergovernmental Panel on Climate Change*, edited by S. Solomon et al., Cambridge Univ. Press, Cambridge.

Jeong, S.-J., C.-H. Ho, T.-W. Park, J. Kim, and S. Levis (2010), Impact of vegetation feedback on the temperature and its diurnal range over the Northern Hemisphere during summer in a 2 × CO_2 climate, *Clim. Dyn.*, doi:10.1007/s00382-010-0827.

Jonko, A. K., K. M. Shell, B. M. Sanderson, and G. Danabasoglu (2012), Climate feedbacks in CCSM3 under changing CO_2 forcing. Part II: Variation of climate feedbacks and sensitivity with forcing, *J. Clim.*, *26*, 2784–2795.

Klein, S. A., et al. (2009), Intercomparison of model simulations of mixed-phase clouds observed during the ARM Mixed-Phase Arctic Cloud Experiment. I: Single-layer cloud, *Q. J. R. Meteorol. Soc.*, *135*, 976–1002.

Le Treut, H., and Z. X. Li (1991), Sensitivity of an atmospheric general circulation model to prescribed SST changes: Feedback effects associated with the simulation of cloud optical properties, *Clim. Dyn.*, *5*, 175–187.

Lee, M.-I., I.-S. Kang, J.-K. Kim, and B. E. Mapes (2001), Influence of cloud-radiation interaction on simulating tropical intraseasonal oscillation with an atmospheric general circulation model, *J. Geophys. Res.*, *106*, 14,219–14,233.

Li, Z. X., and H. Le Treut (1992), Cloud-radiation feedbacks in a general circulation model and their dependence on cloud modeling assumptions, *Clim. Dyn.*, *7*, 133–139.

Lindzen, R. S., and Y.-S. Choi (2009), On the determination of climate feedbacks from ERBE data, *Geophys. Res. Lett.*, *36*, L16705, doi:10.1029/2009GL039628.

Lindzen, R. S., and Y.-S. Choi (2011), On the observational determination of climate sensitivity and its implications, *Asia-Pac. J. Atmos. Sci.*, *47*(4), 377–390.

Lindzen, R. S., A. Y. Hou, and B. F. Farrell (1982), The role of convective model choice in calculating the climate impact of doubling CO_2, *J. Atmos. Sci.*, *39*, 1189–1205.

Liou, K. N. (2002), Presentation of a unified theory for light scattering by ice crystals, in *An Introduction to Atmospheric Radiation*, 2nd ed., pp. 228–234, Elsevier, New York.

Lohmann, U., and C. Hoose (2009), Sensitivity studies of different aerosol indirect effects in mixed-phase clouds, *Atmos. Chem. Phys.*, *9*, 8917–8934.

Mason, B. J. (1957), *The Physics of Clouds*, Clarendon Press, Oxford.

Meehl, G. A., et al. (2007), Global climate projections, in *Climate Change 2007: The Physical Science Basis. Contribution of Working Group I to the Fourth Assessment Report of the Intergovernmental Panel on Climate Change*, edited by S. Solomon et al., pp. 749–845, Cambridge Univ. Press, Cambridge.

Oleson, K. W., et al. (2004), Technical description of the Community Land Model (CLM), *NCAR Tech. Note, NCAR/TN-461+STR*.

Penner, J. E., Y. Chen, M. Wang, and X. Liu (2009), Possible influence of anthropogenic aerosols on cirrus cloud and anthropogenic forcing, *Atmos. Chem. Phys.*, *9*, 879–896.

Pruppacher, H., and J. Klett (1997), *Microphysics of Clouds and Precipitation*, Kluwer Acad., Neth.

Roe, G. H., and M. B. Baker (2007), Why is climate sensitivity so unpredictable?, *Science*, *318*, 629.

Senior, C. A., and F. B. Mitchell (1993), Carbon dioxide and climate: The impact of cloud parameterization, *J. Clim.*, *6*, 393–418.

Shell, K. M., J. T. Kiehl, and C. A. Shields (2008), Using the radiative kernel technique to calculate climate feedbacks in NCAR's Community Atmospheric Model, *J. Clim.*, *21*, 2269–2282.

Smith, R. N. (1990), A scheme for predicting layer clouds and their water content in a general circulation model, *Q. J. R. Meteorol. Soc.*, *116*, 435–460.

Soden, B. J., and T. M. Held (2006), An assessment of climate feedbacks in coupled ocean–atmosphere models, *J. Clim.*, *19*, 3354–3360.

Song, X., G. J. Zhang, and J. L. F. Li (2012), Evaluation of microphysics parameterization for convective clouds in the NCAR Community Atmosphere Model CAM5, *J. Clim.*, *25*, 8568–8590.

Storelvmo, T., J. E. Kristjánsson, and U. Lohmann (2008), Aerosol influence on mixed-phase clouds in CAM-Oslo, *J. Atmos. Sci.*, *65*, 3214–3230.

Sundqvist, H. (1988), Parameterization of condensation and associated clouds in models for weather prediction and general circulation simulation, in *Physically-Based Modeling and Simulation of Climate and Climate Change*, vol. 1, edited by M. E. Schlesinger, pp. 433–461, Kluwer Acad, Dordrecht, Neth.

Tsushima, Y., M. J. Webb, K. D. Williams, B. J. Soden, M. Kimoto, Y. Tsushima, S. Emori, N. Andronova, B. Li, and T. Ogura (2006), Importance of the mixed-phase cloud distribution in the control climate for assessing the response of clouds to carbon dioxide increase: A multi-model study, *Clim. Dyn.*, *27*, 113–126.

Webb, M. J., et al. (2006), On the contribution of local feedback mechanisms to the range of climate sensitivity in two GCM ensembles, *Clim. Dyn.*, *27*, 17–38.

Weidle, F., and H. Wernli (2008), Comparison of ERA40 cloud top phase with POLDER-1 observations, *J. Geophys. Res.*, *113*, D05209, doi:10.1029/2007JD009234.